American Journal of Electrical Power and Energy Systems
2024, Vol. 13, No. 4, pp. 69-82
https://doi.org/10.11648/j.epes.20241304.12

Research Article

Single-Switch Inverter Wireless Charger with Adaptive Constant Current and Constant Voltage Control by Transmitting Side Sensing Load Changes of Receiving Side

Shan Lin[1], Jianfen Zheng[2], Yun Lu[1], Fei Zhao[3], Chunfang Wang[2, *]

[1]Guanzhou Metro Design & Research Institute Co., Ltd., Guanzhou, China
[2]College of Electrical Engineering, Qingdao University, Qingdao, China
[3]Yunlu New Energy Technology Co., Ltd., Qingdao, China

Abstract

Because of its excellent flexibility, security, reliability and convenience, wireless power transfer(WPT) has become a research hotspot at home and abroad. Currently available WPT technology has the broadest application prospects and can be used in consumer electronics, household appliances, medical equipment, electric vehicles and many other fields. In low-power wireless charging systems such as electric bicycles, volume and cost of the receiving side are required to be minimized. However, in traditional receiving side circuit, compensation network, sampling circuit and wireless communication circuit make it difficult to reduce the device size and limit further reduction of cost. Aiming at the above problems, a single-switch LC inverter S-S wireless charging circuit with adaptive constant current (CC) and constant voltage (CV) control by transmitting side sensing load changes of receiving side is proposed. In this paper, load-independent CC and CV characteristics and relationship between auxiliary coil voltage and load voltage are derived. The simplest equivalent model of the proposed circuit is developed, the expression for equivalent input voltage is derived, and the constraints of zero-voltage switching (ZVS) are analyzed. Based on the constraint, an iterative method of variable duty cycle is proposed, which can accurately find the duty cycle range in which the ZVS can be realized as well as the peak resonant current in this range, which provides a reference for parametric design of single-switching circuit. Finally, a 5A/54.6V experimental prototype is built to verify the correctness of the proposed theory.

Keywords

Wireless Power Transfer, Constant Current and Constant Voltage, S-S Compensation Topology, Transmitting Side Auxiliary Coil

1. Introduction

Wireless power transfer (WPT) is currently receiving more and more attention and is widely used in various industries [1-3], such as new energy electric vehicles [4-8], aerospace [9], wearable device [10], automatic guided vehicles (AGV) [11], autonomous underwater vehicles (AUV) [12] and other fields.

At present, the high-frequency inverter circuit of WPT mostly adopts full-bridge inverter circuit, half-bridge inverter circuit and single-switch resonant inverter circuit. For the full-bridge inverter circuit, the circuit scheme is mature [13-16], but there are problems such as complex circuit, high

*Corresponding author: Qduwcf@qdu.edu.cn (Chunfang Wang)

Received: 24 November 2024; **Accepted:** 7 December 2024; **Published:** 25 December 2024

cost, complex controlling, low reliability and straight-through problem between the upper and lower bridge arms of the circuit. For the half-bridge inverter circuit, this circuit has been widely used and researched in enterprises and universities [17, 18]. It has many advantages, such as high gain, high efficiency and all switches can realize ZVS, but there is also the risk of straight-through between the upper and lower bridge arms. And the parameter design is complicated and the cost is high. The single-switch inverter circuit does not have the problem of bridge arm straight-through [19]. It has the advantages of high reliability, low cost and simple structure. It is very suitable for low power charging occasions, such as electric toothbrushes, facial cleansing devices, household lawn mowers and electric bicycles.

In low-power charging applications such as electric bicycles, the coil, circuit and battery package on the receiving side are relatively compact. At the same time, in consideration of the cruising range of the electric bicycle, the circuit volume on the receiving side should be as small as possible [20]. However, there is currently a lack of research on the simplified design of the receiving side of the single-switch circuit. Previously, the receiving side of single-switch circuits used structures such as LCC [21], CLC [22], and CLCL [23]. This leads to an increase in components and the size of the circuit on the receiving side [24]. Based on the LC single-switch circuit, this paper uses S-S compensation topology to achieve constant current and constant voltage output, which not only simplifies the compensation device on the transmitting side, but also achieves lightweight design on the receiving side.

At present, there are six main methods of switching from CC to CV. The first is to carry out precise phase-shift control on the full-bridge circuit through load detection, and realize the switching from CC to CV by changing the inverter output voltage [20, 25]. The second is to use relays to switch the compensation network [21, 25-28]. The third is by changing the switching frequency [22, 23, 29]. The fourth is to use variable inductors/capacitors to achieve CC and CV output by changing the compensation network parameters in real time [30, 31]. The fifth is through the clamp coil, the inherent CC and CV output can be realized without wireless communication [32-34]. The sixth is to control the output voltage by controlled rectifier [35, 36]. For a single-switch circuit, the inverter voltage is independent of duty cycle and is only with the frequency and circuit parameters. There is no way to achieve phase-shift control like a full-bridge circuit. At present, the conversion from CC to CV of a single-switch circuit is realized by topology switching [21] or frequency switching [22, 23]. Topology switching and frequency switching both require wireless communication and battery state-of-charge (SOC) detection on the transmitting and receiving sides [32]. Wireless communication has problems of delay and information loss, and SOC detection will increase the number of receiving side devices and complicate control. To solve this problem, it is proposed to add a small auxiliary coil on the transmitting side to realize the identification and detection of the load voltage, and control the action of the transmitting side relay to realize the switching from CC to CV when the battery is charged to the rated voltage.

At present, there are mainly two methods of analysis on the equivalent voltage source and ZVS margin of single-switch circuits. The first is to equate the single-switch drain-source voltage waveform to the superposition of DC and sinusoidal AC [21, 23]. This method is easy to calculate but this method cannot judge whether ZVS can be realized and calculate the ZVS margin. The second is to establish the minimum equivalent model of a single-switch circuit and calculate the equivalent voltage through the time-domain or complex frequency-domain method [37, 38]. This method can determine whether ZVS can be realized, but only using a constant duty cycle method to calculate the ZVS margin and the peak value of the resonant current, it will cause calculation deviations. This paper designs a calculation method of variable duty cycle, which can judge whether ZVS can be realized, and can accurately calculate the realization range of ZVS and the peak value of resonant current.

The main contributions of this paper are as follows:

1) Propose a single-switch S-S topology adaptive CC and CV wireless charger which senses load voltage changes through a small auxiliary coil on the transmitting side. The proposed topology reduces the receiving side resonant components, volume and cost.
2) A calculation method of variable duty cycle is designed, which can accurately calculate the duty cycle range that can achieve soft switching and the resonant current peak within the range. It provides an accurate reference for circuit parameter design.

The rest of the paper is organized as follows. Section II analyzes the working process of the proposed topology, deduces the CC and CV characteristics of the circuit and the relationship between the auxiliary coil voltage and the load voltage. Section III analyzes the single-switch equivalent input voltage source, and analyzes the ZVS of the circuit. Section IV calculates the ZVS and resonant current of this circuit, and carries on the parameter design. Section V builds a 5A/54.6V, peak power 250W experimental prototype. Section VI summarizes the full paper.

2. Topology Analysis and Compensation Network

Figure 1 shows the topology of the proposed circuit. U_{DC} is a DC voltage source, C_{in} is an input filter capacitor, S is a MOSFET. C_r and L_r are LC networks that ensure the normal operation of a single-switch circuit. C_{P1} and C_{P2} are transmitting-side resonant capacitors. L_P and L_S are the self-inductance of the transmitting coil and receiving coil, L_A is the self-inductance of the transmitting side auxiliary coil. M_{PS} is the mutual inductance between the transmitting coil and the receiving coil, M_{PA} is the mutual inductance between

the transmitting coil and the auxiliary coil, and M_{SA} is the mutual inductance between the receiving coil and the auxiliary coil. C_f is the output filter capacitor, U_B is the voltage across the lithium-ion battery of the electric bicycle. D_A is an auxiliary coil circuit half-wave rectifier diode, C_A is a filter capacitor, R_{A1} and R_{A2} are voltage divider resistors, which are connected to the Schmitt trigger to control the action of the transmitting relay K.

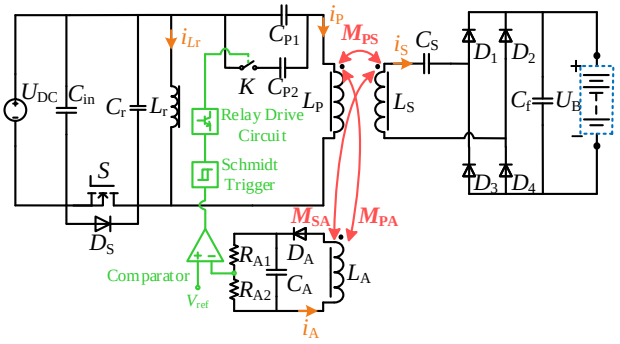

Figure 1. *The proposed circuit topology.*

At the beginning of charging, the control signal of K is low level, K is in the open state, C_{P2} is not connected to the circuit, and the transmitting side resonant capacitor is only C_{P1}, so as to realize constant current charging. As the charging continues, the load voltage U_B increases continuously, so that the voltage across the auxiliary coil increases continuously. When the voltage across the auxiliary coil increases to the set voltage value, the relay K is closed, and C_{P2} is connected in parallel to both sides of C_{P1} to realize a CV output.

The working waveform of the circuit is shown in Figure 2. V_{GS} is the drive signal, V_{DS} is the withstand voltage across the MOSFET, and V_{Cr} is the voltage across the capacitor C_r. i_{Lp}, i_{Lr} and i_{Ls} are the currents flowing through the transmitting coil, inductor L_r and receiving coil respectively.

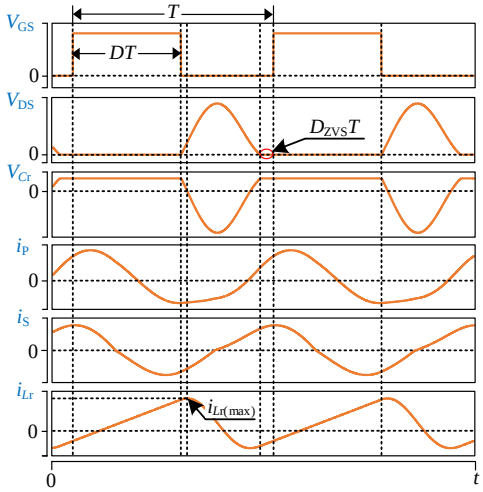

Figure 2. *Working waveform of single-switch circuit.*

2.1. Theoretical Analysis of CC Model

As shown in Figure 3, the IPT system can be equivalent to the controlled source model. $\dot{U}_P$ is the voltage across the capacitor C_r, $\dot{U}_S$ is the input voltage of the rectifier on the receiving side, and $\dot{U}_A$ is the induced voltage across the auxiliary coil L_A. According to Kirchhoff's voltage and current laws, (1) can be obtained

$$\begin{bmatrix} \dot{U}_P \\ \dot{U}_S \\ \dot{U}_A \end{bmatrix} = \begin{bmatrix} j\omega L_P + \dfrac{1}{j\omega C_P} & -j\omega M_{PS} & -j\omega M_{PA} \\ j\omega M_{PS} & -\left(j\omega L_S + \dfrac{1}{j\omega C_S} \right) & -j\omega M_{SA} \\ j\omega M_{PA} & -j\omega M_{SA} & -j\omega L_A \end{bmatrix} \cdot \begin{bmatrix} \dot{I}_P \\ \dot{I}_S \\ \dot{I}_A \end{bmatrix}. \quad (1)$$

In (1), because

$$\dot{I}_A \ll \dot{I}_P, \dot{I}_S \quad (2)$$

thus (1) can be simplified into (3)

$$\begin{bmatrix} \dot{U}_P \\ \dot{U}_S \\ \dot{U}_A \end{bmatrix} = \begin{bmatrix} j\omega L_P + \dfrac{1}{j\omega C_P} & -j\omega M_{PS} \\ j\omega M_{PS} & -\left(j\omega L_S + \dfrac{1}{j\omega C_S} \right) \\ j\omega M_{PA} & -j\omega M_{SA} \end{bmatrix} \cdot \begin{bmatrix} \dot{I}_P \\ \dot{I}_S \end{bmatrix}. \quad (3)$$

From (3) it follows

$$\dot{I}_S = \frac{\left(j\omega L_P + \dfrac{1}{j\omega C_P} \right) \cdot \dot{I}_P - \dot{U}_P}{j\omega M_{PS}}. \quad (4)$$

if

$$j\omega L_P + \frac{1}{j\omega C_P} = 0 \quad (5)$$

then a CC output independent of the load can be achieved

$$\dot{I}_S = -\frac{\dot{U}_P}{j\omega M_{PS}}. \quad (6)$$

2.2. Theoretical Analysis of CV Model

If assume

$$\begin{cases} j\omega\left(L_P-\dfrac{1}{\omega^2 C_P}\right)=Z_P \\ j\omega\left(L_S-\dfrac{1}{\omega^2 C_S}\right)=Z_S \end{cases} \tag{7}$$

then get

$$\begin{aligned} \dot{U}_S &= j\omega M_{PS}\dot{I}_P+\frac{\dot{U}_P-Z_P\dot{I}_P}{j\omega M_{PS}}\cdot Z_S \\ &=\frac{Z_S}{j\omega M_{PS}}\cdot\dot{U}_P+j\omega M_{PS}\left(1+\frac{Z_P Z_S}{\omega^2 M_{PS}^2}\right)\dot{I}_P. \end{aligned} \tag{8}$$

In (8), if let

$$Z_P Z_S=\left(j\omega M_{PS}\right)^2 \tag{9}$$

then a CV output independent of the load can be achieved

$$\dot{U}_S=\frac{Z_S}{j\omega M_{PS}}\cdot\dot{U}_P. \tag{10}$$

According to (10), the voltage gain under CV state is

$$k_{CV}=\frac{j\omega L_S+\dfrac{1}{j\omega C_S}}{j\omega M_{PS}}. \tag{11}$$

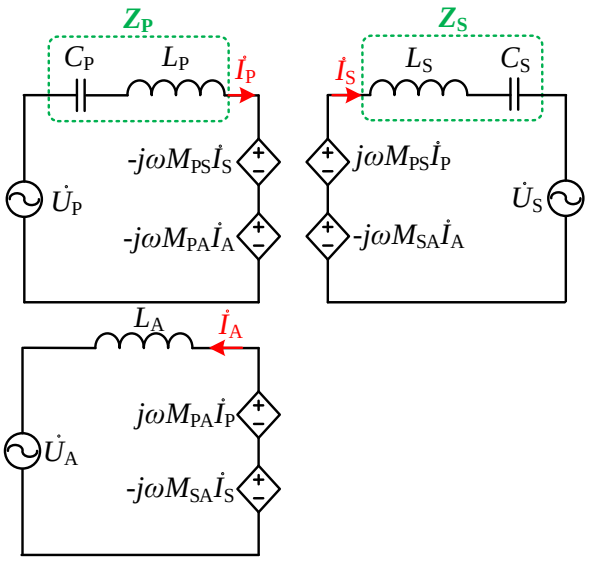

Figure 3. *Controlled source equivalent model of the proposed WPT model.*

2.3. Theoretical Analysis of Transmitting Side Auxiliary Coil

In CC mode, (12) (13) can be obtained from (3)

$$\dot{U}_A=j\omega M_{PA}\dot{I}_P-j\omega M_{SA}\dot{I}_S \tag{12}$$

$$j\omega M_{PS}\dot{I}_P=Z_S\dot{I}_S+\dot{U}_S. \tag{13}$$

Substitute (6) into (13) to get

$$\dot{I}_P=\frac{-\dfrac{Z_S\dot{U}_P}{j\omega M_{PS}}+\dot{U}_S}{j\omega M_{PS}}. \tag{14}$$

Then substitute (14) into (12) to get

$$\dot{U}_A=\left(\frac{M_{SA}}{M_{PS}}-\frac{M_{PA}Z_S}{j\omega M_{PS}^2}\right)\cdot\dot{U}_P+\frac{M_{PA}}{M_{PS}}\cdot\dot{U}_S. \tag{15}$$

And the relationship between the fundamental effective value U_S of $\dot{U}_S$ and the load voltage U_B is

$$U_B=\frac{\pi}{2\sqrt{2}}U_S. \tag{16}$$

From (16), it can be concluded that $\dot{U}_A$ is only related to the load voltage U_B when the mutual inductance is constant. In the electric bicycle charging occasion, the precise alignment between the transmitting coil and the receiving coil can be achieved by means of auxiliary positioning. Therefore, it can be considered that the mutual inductance does not change in actual charging situations.

3. Equivalent Input Voltage Source and Circuit Microscopic Characteristics

3.1. Calculation of Equivalent Input Voltage Source

Before calculating the analytical expression of the equivalent input voltage source of the proposed topology, it is necessary to establish the simplest equivalent circuit. As shown in Figure 4(a), [37] and [38] express the simplest equivalent circuit of a single-switch as a series connection of an inductor and a resistor, which is defined as the C-RL form. However, the simplest equivalent circuit in the form of C-RL cannot correctly reflect the working process of the topology proposed in this article. Therefore, the simplest equivalent circuit in the form of LC-RLC is established as shown in Figure 4(b).

Z_S in Figure 3 generally exhibits inductive properties,

therefore define

$$L_S' = Z_S = L_S - \frac{1}{\omega^2 C_S}. \tag{17}$$

Define Z_{eq} is the impedance equivalent to the transmitting side from the receiving side, and R_L is the load resistance

$$\begin{cases} R_{eq} = \dfrac{8}{\pi^2} R_L \\ Z_{eq} = \dfrac{\omega^2 M_{PS}^2}{Z_S + R_{eq}}. \end{cases} \tag{18}$$

Decomposing Z_{eq} into the form of real and imaginary parts

$$Z_{eq} = \frac{\omega^2 M_{PS}^2 R_{eq}}{R_{eq}^2 + \omega^2 L_S'^2} - j\omega \frac{\omega^2 M_{PS}^2 L_S'}{R_{eq}^2 + \omega^2 L_S'^2}. \tag{19}$$

Then Z_{eq} is equivalent to the transmitting side compensation capacitance and inductance. The RLC series loop is obtained, namely R_e, C_e and L_e.

$$\begin{cases} R_e = \dfrac{\omega^2 M_{PS}^2 R_{eq}}{R_{eq}^2 + \omega^2 L_S'^2} \\ L_e = L_P \\ C_e = \dfrac{\omega^2 M_{PS}^2 L_S'}{R_{eq}^2 + \omega^2 L_S'^2} + \dfrac{1}{C_P}. \end{cases} \tag{20}$$

Establish the complex frequency domain model of the circuit in Figure 4 as shown in Figure 5. MOSFET S has two states of off and on, which are defined as state 1 and state 2 respectively. Take the S turn-off time of each cycle as the starting point of state 1, where U_{Cr1} and U_{Ce1} are the initial voltages of capacitors C_r and C_e, I_{Lr1} and I_{Le2} are the initial currents of inductors L_r and L_e. I_{a1} and I_{b1} are the loop currents of state 1.

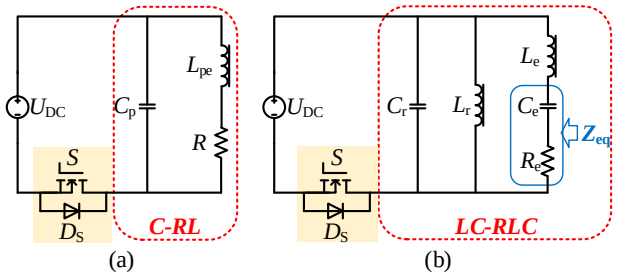

Figure 4. *The simplest equivalent circuit of single-switch topology. (a) C-RL form (b) LC-RLC form.*

According to the complex frequency domain model established in Figure 5, the loop current method is used to obtain the (21).

$$\begin{cases} (\dfrac{1}{sC_r} + sL_r) I_{a1}(s) - sL_r I_{b1}(s) = \dfrac{U_{Cr1}}{s} + L_r I_{Lr1} \\ -sL_r I_{a1}(s) + (sL_r + sL_e + \dfrac{1}{sC_e} + R_e) I_{b1}(s) = -L_r I_{Lr1} + L_e I_{Le1} - \dfrac{U_{Ce1}}{s}. \end{cases} \tag{21}$$

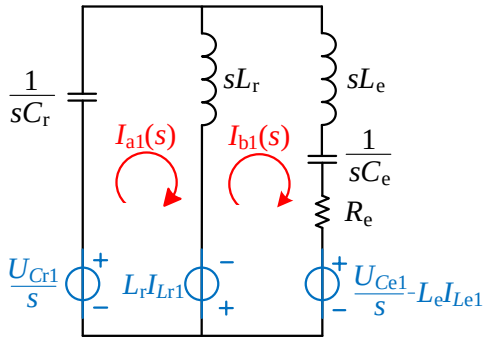

Figure 5. *LC-RLC complex frequency domain model in state 1.*

Then according to the complex frequency domain model diagram, $u_{Cr}(s)$, $u_{Ce}(s)$, $i_{Lr}(s)$ and $i_{Le}(s)$ are obtained. $u_{Cr}(s)$ and $u_{Ce}(s)$ are the complex frequency domain forms of the instantaneous voltage across C_r and C_e, $i_{Lr}(s)$ and $i_{Le}(s)$ are the complex frequency domain forms of the instantaneous current flowing through L_r and L_e.

$$\begin{cases} u_{Cr}(s) = -\dfrac{1}{sC_r} I_{a1}(s) + \dfrac{U_{Cr1}}{s} \\ u_{Ce}(s) = \dfrac{1}{sC_e} I_{b1}(s) + \dfrac{U_{Ce1}}{s} \\ i_{Lr}(s) = I_{a1}(s) - I_{b1}(s) \\ i_{Le}(s) = I_{b1}(s). \end{cases} \tag{22}$$

Then convert the complex frequency domain expressions of $u_{Cr}(s)$, $u_{Ce}(s)$, $i_{Lr}(s)$ and $i_{Le}(s)$ into time domain expressions.

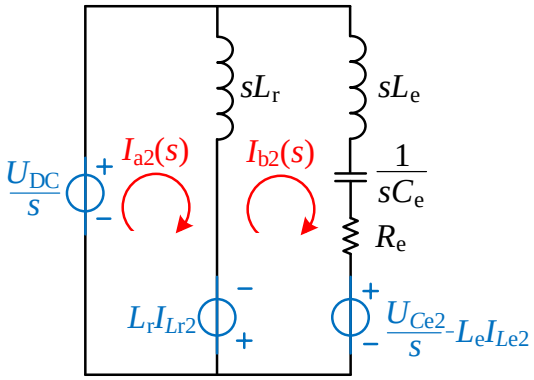

Figure 6. *LC-RLC complex frequency domain model in state 2.*

$$\begin{cases} u_{Cr}(t) = L^{-1}[u_{Cr}(s)] \\ u_{Ce}(t) = L^{-1}[u_{Ce}(s)] \\ i_{Lr}(t) = L^{-1}[i_{Lr}(s)] \\ i_{Le}(t) = L^{-1}[i_{Le}(s)]. \end{cases} \quad (23)$$

At t=(1-D-D_{ZVS})T, let

$$\begin{cases} U_{Cr} = u_{Cr}[(1-D-D_{ZVS})T] \\ U_{Ce} = u_{Ce}[(1-D-D_{ZVS})T] \\ I_{Lr} = i_{Lr}[(1-D-D_{ZVS})T] \\ I_{Le} = i_{Le}[(1-D-D_{ZVS})T]. \end{cases} \quad (24)$$

When the MOSFET S enters the ZVS state, the circuit has actually entered state 2. The complex frequency domain model of the minimum single-switch loop current method is shown in the Figure 6.

According to the complex frequency domain model established in Figure 6, the loop current method is used to obtain the (25). Because the voltage across the capacitor and the current flowing through the inductor cannot change suddenly, according to (24), U_{Cr2} and U_{Ce2} are the initial voltage of capacitor C_r and C_e in state 2, I_{Lr2} and I_{Le2} are the initial currents of inductors L_r and L_e in state 2. I_{a2} and I_{b2} are the loop currents of state 2.

$$\begin{cases} sL_r I_{a2}(s) - sL_r I_{b2}(s) = \dfrac{U_{DC}}{s} + L_r I_{Lr2} \\ -sL_r I_{a2}(s) + (sL_r + sL_e + \dfrac{1}{sC_e} + R_e) I_{b2}(s) = -L_r I_{Lr2} + L_e I_{Le2} - \dfrac{U_{Ce2}}{s}. \end{cases} \quad (25)$$

Then according to the complex frequency domain model diagram, u_{Ce}(s), i_{Lr}(s) and i_{Le}(s) are obtained.

$$\begin{cases} u_{Ce}(s) = \dfrac{1}{sC_e} I_{b2}(s) + \dfrac{U_{Ce2}}{s} \\ i_{Lr}(s) = I_{a2}(s) - I_{b2}(s) \\ i_{Le}(s) = I_{b2}(s). \end{cases} \quad (26)$$

Then convert the complex frequency domain expressions of u_{Ce}(s), i_{Lr}(s) and i_{Le}(s) into time domain expressions

$$\begin{cases} u_{Ce}(t) = L^{-1}[u_{Ce}(s)] \\ i_{Lr}(t) = L^{-1}[i_{Lr}(s)] \\ i_{Le}(t) = L^{-1}[i_{Le}(s)]. \end{cases} \quad (27)$$

Let t=(D+D_{ZVS})T, get the values of u_{Ce}(t), i_{Lr}(t) and i_{Le}(t) at the last moments of state 2. And because the voltage across the capacitor and the current flowing through the inductor cannot change suddenly, the following equation can be established

$$\begin{cases} U_{Cr1} = U_{DC} \\ u_{Ce}[(D+D_{ZVS})T] = U_{Ce2} \\ i_{Lr}[(D+D_{ZVS})T] = I_{Lr2} \\ i_{Le}[(D+D_{ZVS})T] = I_{Le2}. \end{cases} \quad (28)$$

According to (28), the values of I_{Lr1}, I_{Le1}, U_{Ce1} and U_{Cr1} can be obtained when t = 0. So as to solve the time domain equation of u_{Cr}(t), where k = 1, 2, 3...

$$u_{Cr}(t) = \begin{cases} L^{-1}[u_{Cr}(s)], & (k-1)\mathrm{T} < t < (1-D-D_{ZVS})k\mathrm{T} \\ U_{DC}, & (1-D-D_{ZVS})k\mathrm{T} < t < k\mathrm{T}. \end{cases} \quad (29)$$

Then Fourier decomposes the formula of u_{Cr}(t) to extract the fundamental wave component.

$$u_{Cr}(t) = A_0 + A_1\cos(\omega t + \varphi) + \sum_{n=2}^{\infty} A_n \cos(n\omega t + \varphi_n). \quad (30)$$

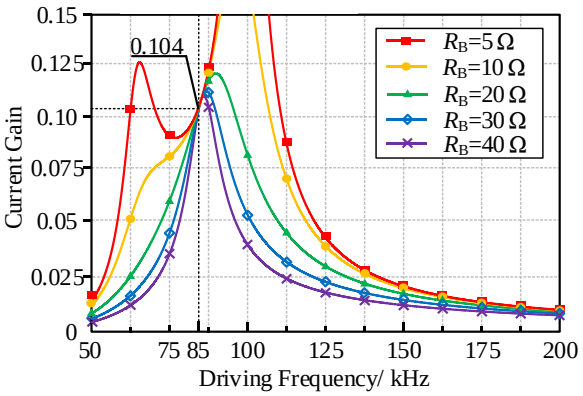

Figure 7. *Relationship between current gain and driving frequency.*

A_0 represents the DC component contained in the waveform, and A_1 represents the amplitude of the fundamental wave

$$\begin{cases} A_1 = \sqrt{a_1^2 + b_1^2} \\ A_0 = a_0. \end{cases} \quad (31)$$

a_0, a_1 and b_1 contained in A_0 and A_1 are determined by (32)

$$\begin{cases} a_0 = \dfrac{1}{T}\int_0^T u_{Cr}(t)dt \\ a_1 = \dfrac{2}{T}\int_0^T u_{Cr}(t)\cos(\omega t)dt \\ b_1 = \dfrac{2}{T}\int_0^T u_{Cr}(t)\sin(\omega t)dt. \end{cases} \quad (32)$$

3.2. Calculation and Characteristics of Current and Voltage Gain

From the (3) in Section II. B, (33) can be obtained:

$$\begin{cases} \dot{I}_S Z_S + \dot{I}_S R_{eq} - j\omega M_{PS}\dot{I}_P = 0 \\ \dot{I}_P Z_P - \dot{U}_P = j\omega M_{PS}\dot{I}_S. \end{cases} \quad (33)$$

(34) can be deduced from (33)

$$\begin{cases} \dot{I}_S = \dfrac{j\omega M_{PS}\dot{I}_P}{R_{eq} + Z_S} \\ \dot{I}_S = \dfrac{\dot{I}_P Z_P - \dot{U}_P}{j\omega M_{PS}}. \end{cases} \quad (34)$$

Combining the two formulas of (34), we can get (35)

$$\dot{I}_P = \frac{R_{eq} + Z_S}{R_{eq}Z_P + Z_P Z_S + \omega^2 M_{PS}^2} \cdot \dot{U}_P. \quad (35)$$

Substituting (35) into (34), we get

$$\dot{I}_S = \frac{j\omega M_{PS}}{Z_P\left(R_{eq} + Z_S\right) + \omega^2 M_{PS}^2} \cdot \dot{U}_P. \quad (36)$$

And the current gain G_{CC} and the voltage gain G_{CV} can be obtained by (37) (38)

$$G_{CC} = \left|\frac{\dot{I}_S}{\dot{U}_P}\right| = \left|\frac{j\omega M_{PS}}{Z_P\left(R_{eq} + Z_S\right) + \omega^2 M_{PS}^2}\right| \quad (37)$$

$$G_{CV} = \left|\frac{\dot{I}_S R_{eq}}{\dot{U}_P}\right| = \left|\frac{j\omega M_{PS} R_{eq}}{Z_P\left(R_{eq} + Z_S\right) + \omega^2 M_{PS}^2}\right|. \quad (38)$$

According to the (37) (38), under different load resistances, the relationship diagram between the current gain G_{CC} and the driving frequency, the relationship diagram between the voltage gain G_{CV} and the driving frequency can be drawn, as shown in Figure 7 and Figure 8.

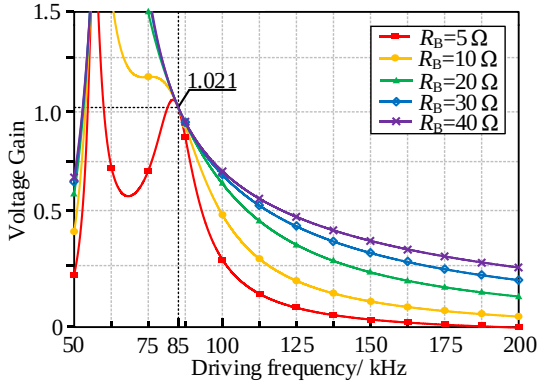

Figure 8. *Relationship between voltage gain and driving frequency.*

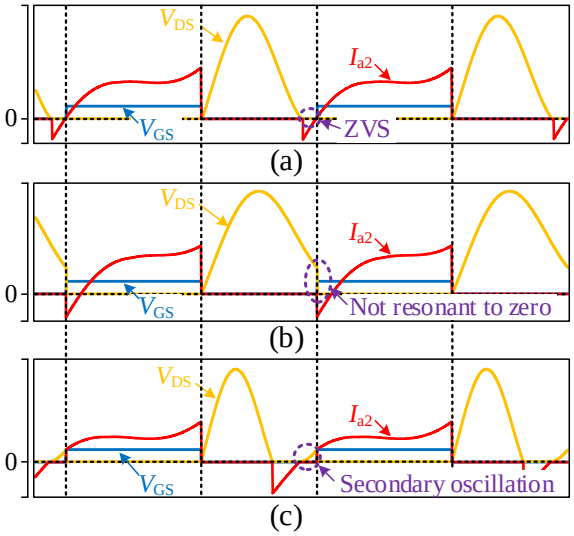

Figure 9. *ZVS of single-switch circuit (a) normal condition (b) V_{DS} cannot be reduced to zero (c) V_{DS} secondary oscillation.*

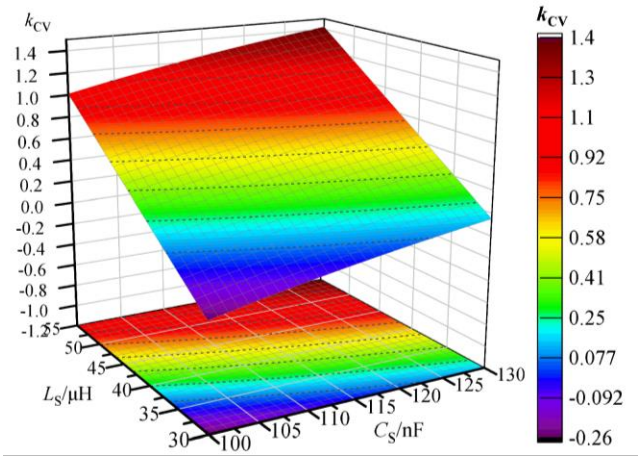

Figure 10. *Relationship between k_{CV} and L_S and C_S.*

Table 1. *Essential parameters of the wpt system.*

Symbol	Definition	Value
U_{DC}	Input DC voltage	48V
f	Operating frequency	85kHz
I_B	Output current in constant-current mode	5.0A
V_B	Output voltage in constant-voltage mode	54.6V
P_B	Output power	250W

3.3. ZVS Analysis

For a single-switch circuit, the V_{DS} waveform mainly presents three forms, as shown in Figure 9. Figure 9 (a) shows the normal operating status of the single-switch circuit with ZVS function. Figure 9 (b) shows the state where V_{DS} will not resonate to zero at all. Figure 9 (c) shows a secondary oscil-

lation phenomenon in V_{DS}. Both Figure 9 (b) and Figure 9 (c) have no ZVS function.

There are two reasons for the phenomenon in Figure 9 (b). The first is that the duty cycle D is set over great, causing the rising edge of V_{GS} to come prematurely. The second is that the value of the resonant capacitor C_r is set over great.

The reason for the phenomenon in Figure 9 (c) is that before the arrival of the drive signal, the current I_{a2} which could flow through the parasitic diode of the MOSFET before, reversed during the resonance process, so that it could not continue to flow through the MOSFET. And the I_{a2} can only be provided by the discharge of capacitor C_r.

Therefore, to determine whether ZVS can be realized, two conditions need to be met at the same time. The first is that there is a zero-crossing point in the V_{DS} waveform, and there is a certain margin around the zero-crossing point. The second is that when the parasitic diode of the MOSFET is in the state 2, the current I_{a2} not higher than zero before the drive signal comes. As shown in (39).

$$\begin{cases} \min[V_{DS}(t)] \le 0 \\ I_{a2}(t)\big|_{t=(1-D-D_{ZVS})T} \le 0. \end{cases} \tag{39}$$

4. The Proposed System Parameter Design

According to the (9) in the Section II. C, if the CV condition is to be realized, Z_P and Z_S must be inductive or capacitive at the same time. If both Z_P and Z_S are capacitive, according to (11), k_{CV} is negative, so Z_P and Z_S must be inductive at the same time. Figure 10 reflects the relationship between k_{CV} and C_S, L_S. Figure 10 shows the variation trend between voltage gain and C_S, L_S.

The essential parameters of the proposed WPT system are shown in Table 1. According to factors such as the voltage gain and the volume of the receiving coil, it is determined that L_S=45μH and C_S=116.4nF. Then determine the coupling coefficient k=0.379 according to the transmission distance and the current gain. And determine L_P and C_P according to (5) (9).

The design of L_r and C_r is related to ZVS margin and maximum resonant current. This paper proposes a computer-aided method to calculate the ZVS margin and the maximum resonant current by changing the duty cycle D. Figure 11 shows a flowchart of this calculation method. D_1 is the maximum duty cycle that can realize ZVS and D_2 is the minimum duty cycle. $D_{ZVSmargin}$ is the duty cycle range which can achieve ZVS. When u_{Cr} crosses zero for the first time, the i_{Lr} value reaches its maximum.

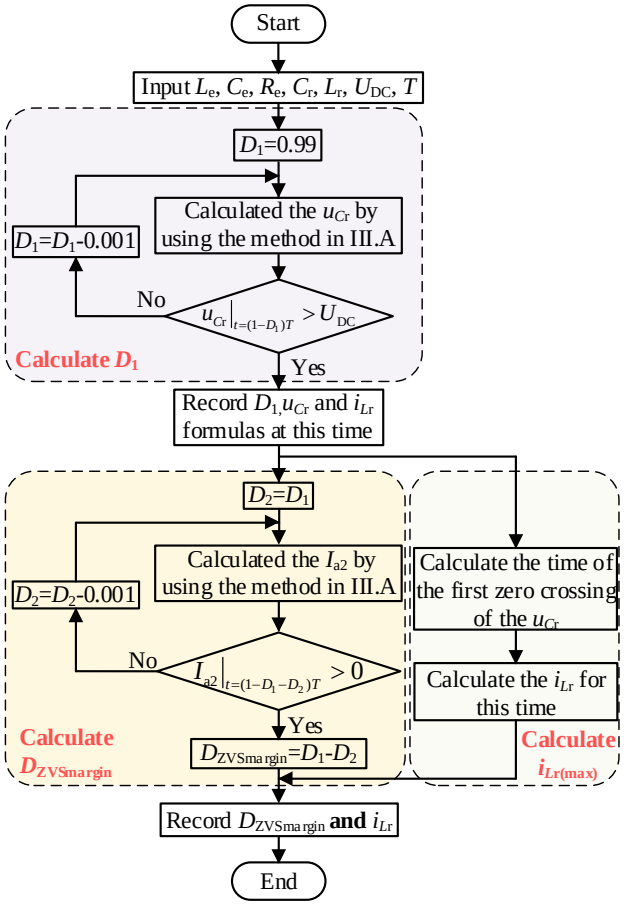

Figure 11. *Flow chart of calculating $D_{ZVSmargin}$ and $i_{Lr(max)}$ with variable duty cycle.*

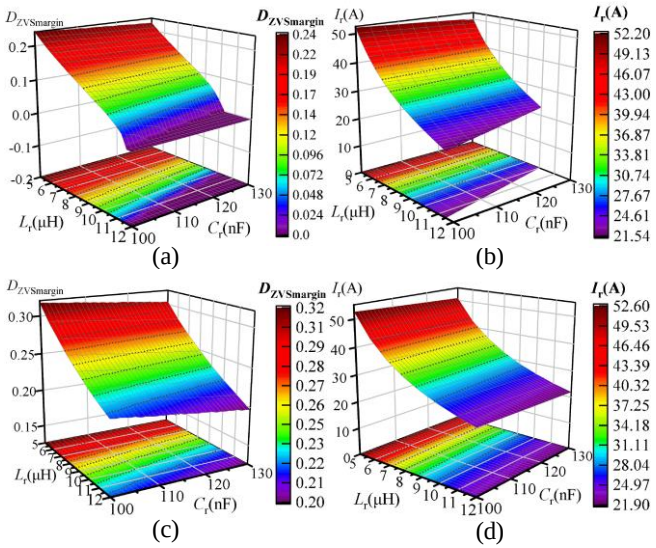

Figure 12. *Relationship between $D_{ZVSmargin}$ and L_S and C_S in (a) CC mode (c) CV mode. Relationship between $i_{Lr(max)}$ and L_S and C_S in (b) CC mode (d) CV mode.*

Table 2. *Parameters of the proposed circuit.*

Symbol	Definition	Value
C_r	Resonant capacitance at the transmitting-side	117.04nF
C_{P1}	Resonant capacitance at the transmitting-side	58.44nF
C_{P2}	Resonant capacitance at the transmitting-side	44.92nF
C_S	Resonant capacitance at the receiving-side	116.51nF
C_A	Auxiliary circuit voltage stabilizing capacitor	19.96 nF
L_r	Resonant inductance at the transmitting-side	9.95μH
L_P	Inductance of the transmitter coil	60.42μH
L_S	Inductance of the receiving coil	45.13μH
L_A	Inductance of the auxiliary coil	5.382μH
N_{LP}	Turns of L_P	23
N_{LS}	Turns of L_S	18
N_{LA}	Turns of L_A	8
M_{PS}	Mutual inductance between L_P and L_S	19.70μH
M_{PA}	Mutual inductance between L_P and L_A	4.2375μH
M_{SA}	Mutual inductance between L_S and L_A	1.595μH
D_{ZVS}	Proportion of ZVS	0.085
D	Duty cycle	0.54
h	Transmission distance	30mm

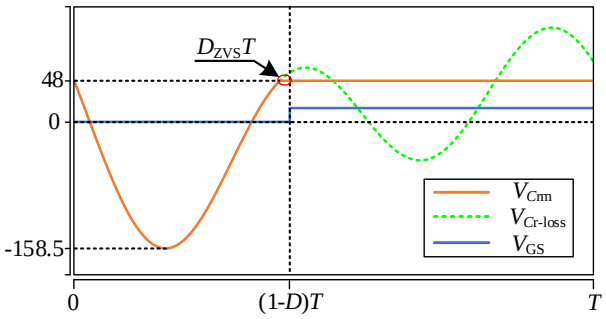

Figure 13. *Mathematica simulates V_{Cr} waveform.*

Calculated according to the method shown in Figure 11, the numerical relationship between $D_{ZVSmargin}$ and L_S, C_S can be obtained, as shown in Figure 12(a) (c). The numerical relationship between the resonance current $i_{Lr(max)}$ and L_S, C_S can also be obtained, as shown in Figure 12(b) (d). Figure 12(a) and Figure 12(b) are in CC mode, Figure 12(c) and Figure 12(d) in CV mode. In the blank part of Figure 12(b), because ZVS is not implemented, the corresponding $i_{Lr(max)}$ cannot be calculated according to the flowchart in Figure 11, and the index has no data. Because it is necessary to minimize the peak value of the resonant current $i_{Lr(max)}$ while ensuring a certain ZVS margin, according to Figure 12, select L_r=10μH and C_r=117nF.

On the basis of the above analysis, the relevant parameters of the proposed circuit topology have been designed, and the actual values of these parameters are shown in Table 2.

In order to verify the correctness of Section III.A., according to the parameters in Table 2 and use the Mathematica software to calculate the V_{Cr} formula in each period. The result is shown in Figure 13. In Figure 13, the V_{Cr} waveform calculated by Mathematica is obtained by adding the V_{Crm} waveform on the left side of (1-D-D_{ZVS})T to the $V_{Cr\text{-}loss}$ waveform. When V_{Cr} resonance rises to 48V, V_{Cr} is clamped to 48V and the $V_{Cr\text{-}loss}$ waveform is discarded. The minimum value of the V_{Cr} waveform in Figure 13 is -158.5V, which is within 0.1V of the simulated value (-158.4V), the error range is 0.63%, while the error range of the [37] is 2.01% (the calculated value in [37] is 295.925V, and the simulated value is 302V).

The structure of the magnetic coupler used in this paper is shown in Figure 14. The gray part is the nanocrystalline, the rose red part is the transmitting side auxiliary coil, and the gold part is the transmitting coil and receiving coil. The relevant parameters of the magnetic coupler have been marked

in Figure 14. The thickness of the nanocrystalline is 0.2mm.

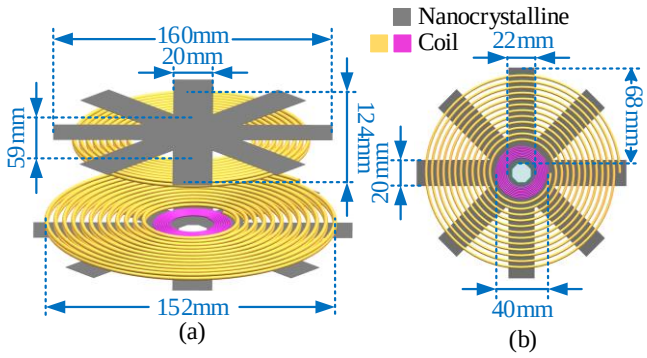

Figure 14. *Magnetic coupler model. (a) Overall view of magnetic coupler (b) top view of transmitting side.*

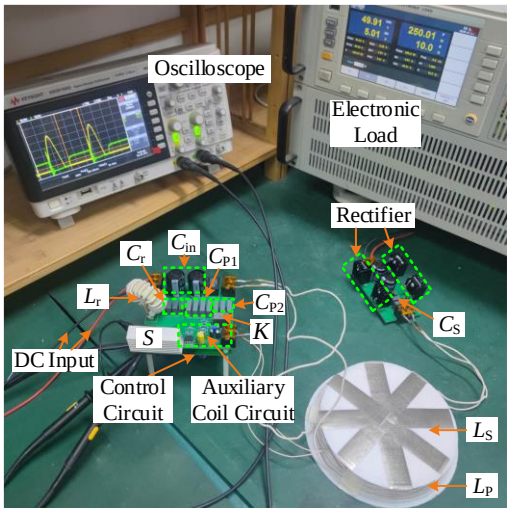

Figure 15. *Photo of the proposed circuit.*

5. Experimental Verification

As shown in Figure 15, in order to verify the correctness of the above analysis, an IPT charger prototype based on S-S compensation was built to charge the lithium-ion battery with a current of 5A and a voltage of 54.6V. Experimental equipment includes transmitting side circuit, receiving side circuit, magnetic coupler, control circuit, oscilloscope, digital multimeter and electronic load. S is a SiC MOSFET FCH023N65S3, the receiving rectification diode is STPS60SM200CW and the transmitting side control chip is STM32F103. Both the transmitting and receiving coils are wound with 200 strands of Litz wire. The mutual inductance, self-inductance and parasitic resistance of the coil are measured with an Agilent 4263B LCR instrument. The transmitting side relay adopts MPD-S-112-A. And the electronic load (IT8616) replaces the lithium-ion battery as the load.

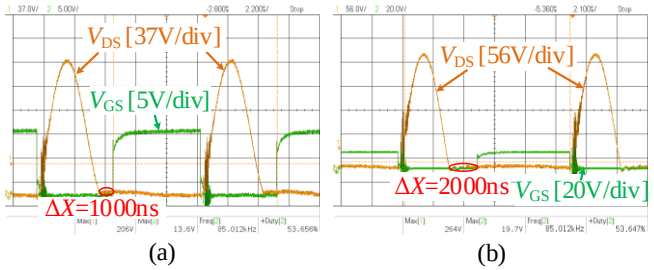

Figure 16. *Switching ZVS and voltage stress waveforms in (a) CC mode, (b) CV mode.*

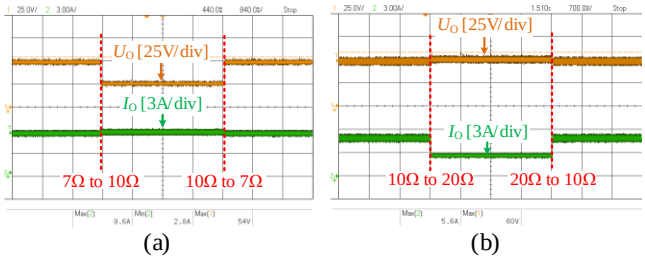

Figure 17. *Variable load experiment (a) CC mode (b) CV mode.*

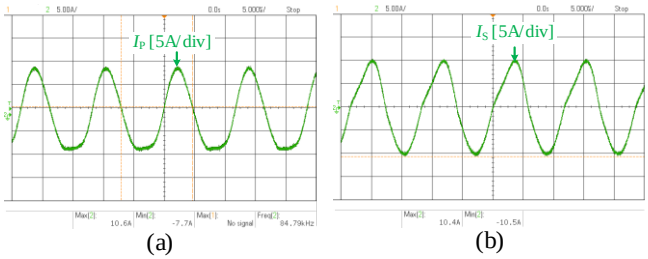

Figure 18. *At rated load R_B=10Ω (a) transmitting coil current I_P (b) receiving coil current I_S.*

As shown in Figure 16(a), the amplitude of MOSFET withstand voltage V_{DS} in CC mode is 206V, and the duty cycle is set to 0.54. The proportion of ZVS in CC mode is 0.085. As shown in Figure 16(b), the amplitude of V_{DS} in CV mode is 264V and the proportion of ZVS is 0.17.

Figure 17 is an experimental waveform of output current I_B and output voltage V_B. In CC mode, when R_B changes from 10Ω to 7Ω, I_B changes from 5.01A to 5.09A. In CV mode, when R_B changes from 10Ω to 20Ω, V_B changes from 49.09 V to 51.83V. Therefore, the circuit has excellent CC and CV characteristics.

When the load is 10Ω, the waveforms of the transmitting coil current I_P and the receiving coil current I_S are shown in Figure 18(a) and Figure 18(b) respectively.

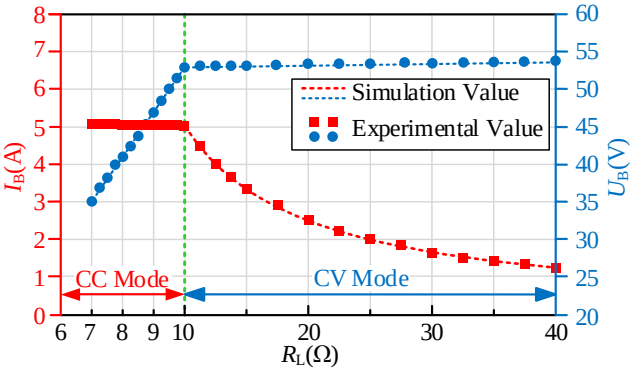

Figure 19. *System CC and CV output.*

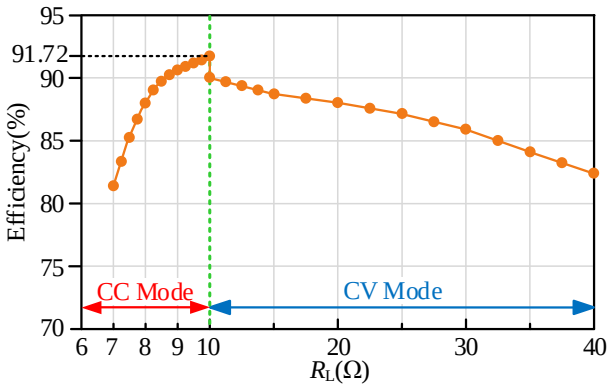

Figure 20. *System efficiency.*

Table 3. *Performance comparison.*

Reference	Input DC Voltage	Frequency	Output Power	Number of MOSFETs	Number of secondary resonant devices	Wireless Communication	CC/CV
Proposed	48V	85kHz	250W	1	1	No	CC and CV
[31]	48V	100kHz	130W	4	1	No	CC and CV
[32]	48V	200kHz	120W	4	2	No	CC and CV
[33]	120V	85kHz	1000W	4	4	No	CC and CV
[35]	200V	85kHz	1050W	6	1	No	CC and CV
[34]	155V	50kHz	1000W	6	1	No	CC and CV
[19]	64V	85kHz	202W	4	1	No	CC and CV
[26]	200V	85kHz	1000W	4	4	/	CC and CV
[22]	24V	100kHz/67kHz	24W	1	4	Yes	CC and CV
[21]	96V	100kHz/86.5kHz	216W	1	3	Yes	CC and CV

Figure 19 shows the relationship between the measured output current and voltage and the load, it can be seen that it has good constant current and constant voltage characteristics. It is worth noting that the application scenario of this article is the 48V lithium-ion battery of an electric bicycle, and the upper limit of the charging voltage is 54.6V. Since the minimum voltage of a single lithium-ion battery is 2.5V, the minimum voltage of the battery pack is 32.5V. Figure 20 shows the system DC-DC efficiency vs load resistance. In CC mode, when R_B=10Ω, the maximum efficiency is 91.72%. When switching to CV mode, as the current flowing through the coil increases, the losses increase, so the efficiency drops at the mode transition.

Table 3 is the comparison between the proposed topology and other literature topologies. It can be seen that the proposed topology has the least number of MOSFETs and the least receiving side compensation components, and has obvious advantages in low-power charging occasions such as electric bicycles.

6. Conclusion

This paper proposed a single-switch inverter wireless charger with adaptive constant current and constant voltage output, which can sense load voltage changes at the transmitting side. The compensation topology of the charger adopts the S-S structure, which reduces the circuit compensation components. At the transmitting side, an auxiliary coil is used to detect load voltage changes. According to the voltage detection result, the transmitting side compensation network is switched through the relay. The charger has the advantages of smooth switching, high voltage detection accuracy, short delay time and low cost. The receiving side circuit has only one compensation capacitor, and has no sampling circuit,

communication circuit or relay. Therefore, it can not only reduce the volume of the receiving side and facilitate the packaging of the circuit and battery, but also reduce the cost of the receiving side. The controlled-source equivalent model of the proposed circuit is established, and the load-independent constant-current and constant-voltage characteristics are deduced. When calculating the ZVS margin and the maximum resonant current of the single-switch circuit, a calculation method of variable duty cycle is used to improve the calculation accuracy. According to the actual lithium-ion battery charging process, a 250W experimental prototype was built, and the maximum efficiency reached 91.72%. The charger can be used in occasions that have strict requirements on the cost and volume of the receiving side, such as electric bicycles. In the future, we can optimize the coil and shielding layer to further reduce the receiving side volume.

Abbreviations

WPT	Wireless Power Transfer Constant Current
CC	Constant Current
CV	Constant Voltage
ZVS	Zero-Voltage Switching

Author Contributions

Shan Lin: Conceptualization, Data curation, Formal Analysis

Jianfen Zheng: Formal Analysis, Methodology, Writing – original draft

Yun Lu: Resources, Software, Validation

Fei Zhao: Resources, Supervision, Visualization

Chunfang Wang: Project administration, Resources, Visualization

Funding

This work was supported in part by the National Natural Science Foundation of China under Grant 51877113, and in part by the Youth Project of Natural Science Foundation of Shandong Province under Grant ZR2023QE298.

Conflicts of Interest

The authors declare no conflicts of interest.

References

[1] Y. Shao, H. Zhang, M. Liu, and C. Ma, "Explicit Design of Impedance Matching Networks for Robust MHz WPT Systems With Different Features," *IEEE Trans. Power Electron.* vol. 37, no. 9, pp. 11382-11393, 2022. https://doi.org/10.1109/TPEL.2022.3165296

[2] Z. Wei, B. Zhang, S. Lin, and C. Wang, "A Self-oscillation WPT System with High Misalignment Tolerance," *IEEE Trans. Power Electron.*, early access, https://doi.org/10.1109/TPEL.2023.3327096

[3] H. Yang *et al.*, "A Hybrid Load Matching Method for WPT Systems to Maintain High Efficiency Over Wide Load Range," *IEEE Trans. Transp. Electrification.* vol. 9, no. 1, pp. 1993-2005, 2023. https://doi.org/10.1109/TTE.2022.3199090

[4] Q. Deng *et al.*, "Wired/Wireless Hybrid Charging System for Electrical Vehicles With Minimum Rated Power Requirement for DC Module," *IEEE Trans. Veh. Technol.* vol. 69, no. 10, pp. 10889-10898, 2020. https://doi.org/10.1109/TVT.2020.3019787

[5] A. Hossain, P. Darvish, S. Mekhilef, K. S. Tey, and C. W. Tong, "A New Coil Structure of Dual Transmitters and Dual Receivers With Integrated Decoupling Coils for Increasing Power Transfer and Misalignment Tolerance of Wireless EV Charging System," *IEEE Trans. Ind. Electron.* vol. 69, no. 8, pp. 7869-7878, 2022. https://doi.org/10.1109/TIE.2021.3108697

[6] S. Zhao, C. Xia, Z. Yang, H. Lu, H. Zhang, and C. Lu, "Bipolar Checkerboard Metal Object Detection Without Blind Zone Caused by Excitation Magnetic Field for Stationary EV Wireless Charging System," *IEEE Trans. Power Electron.* vol. 38, no. 5, pp. 6696-6709, 2023. https://doi.org/10.1109/TPEL.2023.3239117

[7] I. U. Castillo-Zamora, P. S. Huynh, D. Vincent, F. J. Perez-Pinal, M. A. Rodriguez-Licea, and S. S. Williamson, "Hexagonal Geometry Coil for a WPT High-Power Fast Charging Application," *IEEE Trans. Transp. Electrification.* vol. 5, no. 4, pp. 946-956, 2019. https://doi.org/10.1109/TTE.2019.2941636

[8] Y. Wu, C. Liu, M. Zhou, X. Mao, and Y. Zhang, "An Antioffset Electric Vehicle Wireless Charging System Based on Dual Coupled Antiparallel Coils," *IEEE Trans. Power Electron.* vol. 38, no. 5, pp. 5634-5637, 2023. https://doi.org/10.1109/TPEL.2023.3238353

[9] K. Song *et al.*, "A Rotation-Lightweight Wireless Power Transfer System for Solar Wing Driving," *IEEE Trans. Power Electron.* vol. 34, no. 9, pp. 8816-8830, Sep 2019. https://doi.org/10.1109/TPEL.2018.2886910

[10] S. Jeong *et al.*, "Smartwatch Strap Wireless Power Transfer System With Flexible PCB Coil and Shielding Material," *IEEE Trans. Ind. Electron.* vol. 66, no. 5, pp. 4054-4064, May 2019. https://doi.org/10.1109/TIE.2018.2860534

[11] S. Pan, Y. Xu, Y. Lu, W. Liu, Y. Li, and R. Mai, "Design of Compact Magnetic Coupler With Low Leakage EMF for AGV Wireless Power Transfer System," *IEEE Trans. Ind. Appl.* vol. 58, no. 1, pp. 1044-1052, Jan 2022. https://doi.org/10.1109/TIA.2021.3119906

[12] Y. Wang, T. Li, M. Zeng, J. Mai, P. Gu, and D. Xu, "An Underwater Simultaneous Wireless Power and Data Transfer System for AUV With High-Rate Full-Duplex Communication," *IEEE Trans. Power Electron.* vol. 38, no. 1, pp. 619-633, 2023. https://doi.org/10.1109/TPEL.2022.3203038

[13] Y. Chen *et al.*, "A Clamp Circuit-Based Inductive Power Transfer System With Reconfigurable Rectifier Tolerating Extensive Coupling Variations," *IEEE Trans. Power Electron.*, https://doi.org/10.1109/TPEL.2023.3303487

[14] H. Shen, P. Tan, B. Song, X. Gao, and B. Zhang, "Receiver Position Estimation Method for Multitransmitter WPT System Based on Machine Learning," *IEEE Trans. Ind. Appl.* vol. 58, no. 1, pp. 1231-1241, 2022. https://doi.org/10.1109/TIA.2021.3103489

[15] W. Zhong, H. Li, S. Y. R. Hui, and M. D. Xu, "Current Overshoot Suppression of Wireless Power Transfer Systems With on–off Keying Modulation," *IEEE Trans. Power Electron.* vol. 36, no. 3, pp. 2676-2684, 2021. https://doi.org/10.1109/TPEL.2020.3012949

[16] S. Luo, Z. Yao, Z. Zhang, X. Zhang, and H. Ma, "Balanced Dual-Side LCC Compensation in IPT Systems Implementing Unity Power Factor for Wide Load Range and Misalignment Tolerance," *IEEE Trans. Ind. Electron.* vol. 70, no. 8, pp. 7796-7809, 2023. https://doi.org/10.1109/TIE.2022.3224174

[17] S. Samanta, A. K. Rathore, and D. J. Thrimawithana, "Bidirectional Current-Fed Half-Bridge (C) (LC)-(LC) Configuration for Inductive Wireless Power Transfer System," *IEEE Trans. Ind. Appl.* vol. 53, no. 4, pp. 4053-4062, Jul-Aug 2017. https://doi.org/10.1109/TIA.2017.2682793

[18] C. Qi, G. Zheng, Y. Liu, J. Liang, H. Wang, and M. Fu, "A Simplified Three-Order Small-Signal Model for Capacitive Power Transfer System Using Series Compensation," *IEEE Trans. Power Electron.* vol. 38, no. 5, pp. 5688-5692, 2023. https://doi.org/10.1109/TPEL.2023.3243134

[19] H. Yuan, C. Wang, and D. Xia, "Research on Input-Parallel Single-Switch WPT System With Load-Independent Constant Voltage Output," *IEEE Trans. Transp. Electrification.* vol. 9, no. 1, pp. 1888-1896, 2023. https://doi.org/10.1109/TTE.2022.3172328

[20] Z. Li, H. Liu, Y. Tian, and Y. Liu, "Constant Current/Voltage Charging for Primary-Side Controlled Wireless Charging System Without Using Dual-Side Communication," *IEEE Trans. Power Electron.* vol. 36, no. 12, pp. 13562-13577, Dec 2021. https://doi.org/10.1109/TPEL.2021.3088272

[21] Q. Zhang *et al.*, "Research on Input-Parallel Single-Switch Wireless Power Transfer System With Constant-Current and Constant-Voltage Output," *IEEE Trans. Power Electron.* vol. 37, no. 4, pp. 4817-4830, Apr 2022. https://doi.org/10.1109/TPEL.2021.3118434

[22] J. Wang, C. Wang, Z. Lu, Z. Guo, and S. Wang, "Single-Switch Wireless-Power-Transfer Circuit With P-CLC Compensation Network Used for Battery Charging," *IEEE Trans. Transp. Electrification.* vol. 8, no. 3, pp. 4014-4026, Sep 2022. https://doi.org/10.1109/TTE.2022.3160225

[23] R. Yue, C. Wang, H. Li, and Y. Liu, "Constant-Voltage and Constant-Current Output Using P-CLCL Compensation Circuit for Single-Switch Inductive Power Transfer," *IEEE Trans. Power Electron.* vol. 36, no. 5, pp. 5181-5190, May 2021. https://doi.org/10.1109/TPEL.2020.3028128

[24] A. Bharadwaj, A. Sharma, and C. C. Reddy, "An Unconventional Measurement Technique to Estimate Power Transfer Efficiency in Series–Series Resonant WPT System Using S-Parameters," *IEEE Transactions on Instrumentation and Measurement* vol. 71, pp. 1-9, 2022. https://doi.org/10.1109/TIM.2022.3181291

[25] Y. Li *et al.*, "A New Coil Structure and Its Optimization Design With Constant Output Voltage and Constant Output Current for Electric Vehicle Dynamic Wireless Charging," *IEEE Trans. Ind. Inform.* vol. 15, no. 9, pp. 5244-5256, Sep 2019. https://doi.org/10.1109/TII.2019.2896358

[26] H. Li, Y. Yang, J. Chen, J. Xu, M. Liu, and Y. Wang, "A Hybrid Class-E Topology With Constant Current and Constant Voltage Output for Light EVs Wireless Charging Application," *IEEE Trans. Transp. Electrification.* vol. 7, no. 4, pp. 2168-2180, Dec 2021. https://doi.org/10.1109/TTE.2021.3083363

[27] D. Wang, X. Qu, Y. Yao, and P. Yang, "Hybrid Inductive-Power-Transfer Battery Chargers for Electric Vehicle Onboard Charging With Configurable Charging Profile," *IEEE Trans. Intell. Transp. Syst.* vol. 22, no. 1, pp. 592-599, Jan 2021. https://doi.org/10.1109/TITS.2020.2976647

[28] Y. Zhang, Z. Shen, W. Pan, H. Wang, Y. Wu, and X. Mao, "Constant Current and Constant Voltage Charging of Wireless Power Transfer System Based on Three-Coil Structure," *IEEE Trans. Ind. Electron.* vol. 70, no. 1, pp. 1066-1070, Jan 2023. https://doi.org/10.1109/TIE.2022.3150112

[29] J. Cai, X. Wu, P. Sun, Q. Deng, J. Sun, and H. Zhou, "Design of Constant-Voltage and Constant-Current Output Modes of Double-Sided LCC Inductive Power Transfer System for Variable Coupling Conditions," *IEEE Trans. Power Electron.* vol. 39, no. 1, pp. 1676-1689, Jan 2024. https://doi.org/10.1109/TPEL.2022.3226756

[30] Z. Luo, Y. Zhao, M. Xiong, X. Wei, and H. Dai, "A Self-Tuning LCC/LCC System Based on Switch-Controlled Capacitors for Constant-Power Wireless Electric Vehicle Charging," *IEEE Trans. Ind. Electron.* vol. 70, no. 1, pp. 709-720, Jan 2023. https://doi.org/10.1109/TIE.2022.3153812

[31] X. Zhu *et al.*, "High-Efficiency WPT System for CC/CV Charging Based on Double-Half-Bridge Inverter Topology With Variable Inductors," *IEEE Trans. Power Electron.* vol. 37, no. 2, pp. 2437-2448, Feb 2022. https://doi.org/10.1109/TPEL.2021.3107461

[32] Z. Huang, G. Wang, J. Yu, and X. Qu, "A Novel Clamp Coil Assisted IPT Battery Charger With Inherent CC-to-CV Transition Capability," *IEEE Trans. Power Electron.* vol. 36, no. 8, pp. 8607-8611, Aug 2021. https://doi.org/10.1109/TPEL.2021.3107461

[33] G. Li and H. Ma, "A Hybrid IPT System With High-Misalignment Tolerance and Inherent CC-CV Output Characteristics for EVs Charging Applications," *IEEE J. Emerg. Sel. Topics Power Electron.* vol. 10, no. 3, pp. 3152-3160, Jun 2022. https://doi.org/10.1109/JESTPE.2021.3112969

[34] C. Ma, R. Yao, C. Li, and X. Qu, "A Family of IPT Battery Chargers With Small Clamp Coil for Configurable and Self-Sustained Battery Charging Profile," *IEEE Trans. Power Electron.* vol. 38, no. 6, pp. 7910-7919, Jun 2023. https://doi.org/10.1109/TPEL.2023.3257372

[35] I. W. Iam *et al.*, "Constant-Frequency and Noncommunication-Based Inductive Power Transfer Converter for Battery Charging," *IEEE J. Emerg. Sel. Topics Power Electron.* vol. 10, no. 2, pp. 2147-2162, Apr 2022. https://doi.org/10.1109/JESTPE.2020.3004259

[36] V. Yenil and S. Cetin, "Load Independent Constant Current and Constant Voltage Control of LCC-Series Compensated Wireless EV Charger," *IEEE Trans. Power Electron.* vol. 37, no. 7, pp. 8701-8712, Jul 2022. https://doi.org/10.1109/TPEL.2022.3144160

[37] Z. Guo, C. Wang, S. Lin, L. Yang, and X. Lu, "Multiparallel and Flexible Expansion of Single-Switch WPT Inverter by Magnetic Integration," *IEEE Trans. Power Electron.* vol. 38, no. 3, pp. 4167-4180, Mar 2023. https://doi.org/10.1109/TPEL.2022.3221973

[38] G. Ke, Q. Chen, S. Zhang, X. Xu, and L. Xu, "A Single-Ended Hybrid Resonant Converter With High Misalignment Tolerance," *IEEE Trans. Power Electron.* vol. 37, no. 10, pp. 12841-12852, Oct 2022. https://doi.org/10.1109/TPEL.2022.3173633